First-principles Modeling of IAT-driven Anomalous Resistivity in Hollow Cathode Discharges II: Numerical Simulations and Comparisons with Experiments

Alejandro Lopez Ortega[1], Ioannis G. Mikellides[2] and Benjamin A. Jorns[3]
Jet Propulsion Laboratory, California Institute of Technology, Pasadena, CA, 91107, USA

We present a model that quantifies the magnitude of the ion-acoustic turbulence (IAT) in the plume of hollow cathodes and its effect on the resistivity and ion heating. The model takes the form of a partial differential equation (PDE) that can be solved concurrently with the equations of motion for a partially ionized plasma already included in our numerical code for the simulation of the plasma discharge in hollow cathodes, OrCa2D. We also determine that self-induced magnetic fields are not negligible in hollow cathodes operating at large discharge currents and implement in our code Ampere's law and modifications to Ohm's law that account for this effect. Numerical simulations that employed these models show large improvements in our agreement with experimental measurements with respect to a previous model, which assumed complete saturation of the IAT and did not account for the growth stage of the waves. In particular, the model is able to accurately predict the location and magnitude of the maximum resitivity to the electron current along the cathode centerline.

Nomenclature

$\mathbf{B}$	=	magnetic field (vector)
B	=	magnetic field (magnitude)
β	=	unitary vector in direction of magnetic field
c	=	sound speed
e	=	electron charge
$\mathbf{E}$	=	electric field vector
ε_{ip}	=	ionization potential
γ	=	growth rate of oscillation
$\mathbf{j}$	=	current density vector
k	=	wave-length
κ	=	thermal conductivity
L_{em}	=	emitter length
λ_D	=	Debye length
m	=	molecular mass
M	=	Mach number
μ_0	=	vacuum permeability
n	=	number density
N_k	=	wave action
η	=	resistivity
p	=	pressure

[1] Member of the Technical Staff, Electric Propulsion Group, 4800 Oak Grove Drive, Pasadena, CA, 91109, Mail Stop 125-109, Member AIAA.
[2] Principal Engineer, Electric Propulsion Group, 4800 Oak Grove Drive, Pasadena, CA, 91109, Mail Stop 125-109, Associate Fellow AIAA.
[3] Member of the Technical Staff, Electric Propulsion Group, 4800 Oak Grove Drive, Pasadena, CA, 91109, Mail Stop 125-109, Member AIAA.
Copyright 2016 California Institute of Technology. U.S. Government sponsorship acknowledged.

ϕ	=	plasma potential
φ_{wF}	=	work function of emitter
φ_{SH}	=	change in work function due to Shottky effect
Q^R	=	friction heating
Q^T	=	thermal heating
r	=	coordinate in radial direction
t	=	time
T	=	temperature
T_w	=	emitter wall temperature
θ	=	coordinate in azimuthal direction
$\boldsymbol{\tau}$	=	viscous stress tensor
$\mathbf{u}$	=	velocity vector
ν	=	collision frequency
W_T	=	wave energy density
W_0	=	floor value of the wave energy density
ω_p	=	plasma frequency
ω	=	frequency of oscillation
z	=	coordinate in axial direction
a	=	(subscript) anomalous
e	=	(subscript) electron
i	=	(subscript) ion
n	=	(subscript) neutral
//	=	(subscript) parallel to magnetic field
$\perp$	=	(subscript) perpendicular to magnetic field

I. Introduction

Electric propulsion systems have been proposed as the main propulsion source for deep space exploration missions. The power, throughput, and life requirements for these deep space missions exceed those needed for the station-keeping and orbit-raising maneuvers in Earth orbit for which electric propulsion systems have mainly been used in the past. For instance, the proposed Asteroid Robotic Redirect Mission (ARRM) would require power and operating times in the order of 30 kW and 30,000 hours, respectively [1-2]. Hollow cathodes, in which a propellant gas flow (typically xenon) is introduced into the cathode tube, are commonly used as the source of electrons for plasma propulsion devices, such as Hall thrusters. A well-known failure mechanism in hollow cathodes is the erosion of the cathode keeper (a metallic piece that protects the cathode structure from ion bombardment) [3-4]. The principal cause of keeper erosion has been identified as the sputtering by ions with energies that exceed the discharge voltage. Thus, keeper erosion has been prevented in the past by employing materials with lower sputtering yield and by avoiding an operating condition known as “plume mode” [5], whose characteristic feature is the presence of large global oscillations in the plume of the cathode. Even though the driving mechanism for plume mode is not completely understood, it has been shown experimentally that it can be avoided by increasing the mass flow of propellant gas into the cathode. While the employment of these techniques produced successful results in low-current cathodes (<20 A), it has been unclear until recently how the required increase in generated current imposed by high-power space exploration missions would affect the degradation mechanisms in hollow cathodes.

Mikellides et al. [6] postulated that the presence of anomalous resistivity in the plume of a hollow cathode was required to explain the increase in plasma potential and electron heating that occurs downstream of the cathode orifice. It was also pointed out in [7-8] by means of numerical simulations and analysis that the conditions for growth of ion-acoustic turbulence (IAT) [9-12] existed downstream of the cathode exit orifice. This instability occurs when the drift velocity of electrons exceeds the thermal speed. The conditions for the inception of IAT also take place in cathodes with larger discharge currents (in the vicinity of 100 A). It was also shown that the anomalous resistivity of the electrons subjected to IAT is sufficient to explain the electron temperature and plasma potential profiles observed in the cathode plume. A second effect of the IAT is the formation of a high-energy tail in the distribution function of the ions. These high energy ions can impact the keeper surface, producing erosion. Experimental confirmation of the presence of IAT in the cathode plume was first reported for a high-current lanthanum hexaboride (LaB_6) cathode by Jorns et al. [13]. As an example of a mitigation technique, a parametric study of the magnitude of the turbulence as a function of the discharge current and mass flow rate of xenon revealed specific mass flow rates at discharge currents in excess of 25 A for which the amplitude of the turbulent oscillations were minimal.

Driven largely by a need to understand the evolution of the partially ionized gas inside hollow cathodes, which is inherently difficult to access with diagnostcis, development of Orificed Cathode 2D (OrCa2D) began in mid-2000 [6,8,14-16]. This numerical code was actively used in the investigations that led to determining that the conditions for the growth of IAT existed downstream of the cathode exit orifice. OrCa2D is a first-principles numerical code, based on the fluid approximation for the motion of ions and electrons, that simulates the plasma conditions inside the cathode and in the cathode plume. The presence of ion-acoustic turbulence in cathode plumes is modeled as an additional "anomalous collision frequency" that contributes to the resistitivity of electrons. We have used an algebraic model to determine this term that has been derived from Sagdeev and Galev [17] and assumes that the IAT has reached the saturation stage. We have found that even though this model produces plasma parameters that are qualitatively in accordance with the experiments, it is not entirely accurate in the vicinity of the cathode orifice, where the instability develops. This characteristic becomes more acute in high-current cathodes.

The aim of OrCa2D is to serve as a tool that can guide the design and predict the service life of new hollow cathodes. Improvements in the physics models of OrCa2D reduce uncertainties in the predictions produced by the code. In this article, we present the results of implementing a model for the IAT that stems directly from kinetic theory and the notion that waves can be described as quasi-particles [18]. It takes the form of a partial differential equation (PDE) instead of the algebraic expression used to date [16]. This PDE is solved concurrently with the evolution equations for neutrals, ions, and electrons. The derivation of this model has been described in our companion paper [19]. In Section II, we provide a summary of the models included in OrCa2D, including the evolution equation for the IAT. Comparisons between experimental measurements and numerical results are shown in Section III for a high current LaB_6 cathode operating at 140 A and 10 sccm. We find that self-induced magnetic fields are not negligible in cathodes operating at large dischrarge currents. Section IV presents the modifications to the equations of motion that are required to account for self-induced magnetic fields and shows that agreement of numerical results with experimental measurements improve after these changes have been introduced. In Section V, we explore the effect of accounting for the ion heating that results from the ion-acoustic turbulence. In order to do this, we follow recent experimental measurements that suggest that the ion temperature increases proportionally to the magnitude of the turbulence in the plasma. Section VI summarizes the main findings in this article.

II. Numerical model in OrCa2D

The physics models and numerical methods in OrCa2D have been described in detail in [6,8,14-16] and will only be described briefly here. OrCa2D solves conservation laws for the three species present in a partially ionized gas: electrons, xenon ions, and xenon neutrals. A time-splitting method in which all the equations are solved consecutively at every time-step is employed. Inside the cathode, the Navier-Stokes equations for neutral xenon (1-2) are solved using an implicit backward Euler scheme, which includes the viscous terms. It has been shown that the flow of neutrals transitions from a low to a high Knuden number downstream of the cathode orifice. Thus, a fluid approximation is not applicable in the cathode plume. Free molecular flow, in which neutrals move in straight paths, is assumed downstream of an axial location, typically chosen to be in the cathode orifice where the Knudsen number approaches unity. Mass and momentum continuity is preserved across the transition boundary. The Euler equations for mass and momentum of charged ions (3-4) are solved in the entire computational domain. The presence of ion momentum terms was recently included to account for the increased ion densities and currents in high-current cathodes. The effects of ionization, charge exchange and electron-ion collisions are considered in the equations and modeled as source or drag terms. The conservation equations for ions are also solved using a backward Euler implicit scheme. Previous studies [14,16] have shown that the thermal equilibration time between ions and neutrals is small, which allows for solving only one energy equation for both ions and neutrals (5). Finally, the plasma parameters for electrons are determined from the solution of the electron energy equation (6), which also employs a backward Euler scheme, and the combination of the current conservation equation (8) with the vector form of Ohm's law (7). The resisitivity η in Ohm's law (9) is determined as a function of the classical collision frequencies (i.e., electron-ion and electron-neutral) and the anomalous collision frequency that models the effect of the IAT on the electron transport. When an external magnetic field is applied, the resistivity is no longer isotropic, with the component perpendicular to the magnetic field dependent on the electron Hall parameter Ω_e. The modeling of the anomalous collision frequency will be shown in Subsection IIIa.

$$\frac{\partial n_n}{\partial t} + \nabla \cdot \left(n_n \mathbf{u}_n \right) = -\dot{n}, \tag{1}$$

$$\frac{\partial \left(mn\mathbf{u} \right)_n}{\partial t} + \nabla \cdot \left(mn\mathbf{u}\mathbf{u} \right)_n = mn\nu_{in}\left(\mathbf{u}_i - \mathbf{u}_n \right) - \nabla p_n + \nabla \cdot \overline{\boldsymbol{\tau}}, \tag{2}$$

$$\frac{\partial n}{\partial t}+\nabla\cdot(n\mathbf{u}_i)=\dot{n},\quad n_e=n_i, \tag{3}$$

$$\frac{\partial(mn\mathbf{u})_i}{\partial t}+\nabla\cdot(mn\mathbf{u}\mathbf{u})_i=ne\mathbf{E}-\nabla p_i+\dot{n}\mathbf{u}_n-nm\left[\nu_{ie}(\mathbf{u}_i-\mathbf{u}_e)+\nu_{in}(\mathbf{u}_i-\mathbf{u}_n),\right] \tag{4}$$

$$\frac{3}{2}\frac{\partial p_{i,n}}{\partial t}+\nabla\cdot\left(\frac{5}{2}p_{i,n}\mathbf{u}_{i,n}-\kappa_{i,n}\nabla T_{i,n}\right)=Q_{i,n}^R+Q_{i,n}^T+\mathbf{u}_{i,n}\cdot\nabla p_{i,n}, \tag{5}$$

$$\frac{3}{2}\frac{\partial p_e}{\partial t}-\nabla\cdot\left(\frac{5}{2}T_e\mathbf{j}_e+\kappa_e\nabla T_e\right)=Q_e^R+Q_e^T-\mathbf{j}_e\cdot\frac{\nabla p_e}{en}-\dot{n}e\varepsilon_{ip}, \tag{6}$$

$$0=-ne\mathbf{E}-ne\mathbf{u}_e\times\mathbf{B}-\nabla p_e-nm_e\left[\nu_{ei}(\mathbf{u}_e-\mathbf{u}_i)+\nu_{en}\mathbf{u}_e\right],\qquad \mathbf{u}_e>>\mathbf{u}_n, \tag{7}$$

$$\nabla\cdot(\mathbf{j}_e+\mathbf{j}_i)=0\rightarrow$$

$$\nabla\cdot\left[\frac{\nabla\phi}{\eta}-\frac{\nabla p_e}{\eta en}-\mathbf{j}_i\left(1-\frac{\nu_{ei}}{\nu_{en}+\nu_{ei}}\right)\right]=0, \tag{8}$$

$$\eta_{//}=\frac{m_e(\nu_{en}+\nu_{ei}+\nu_a)}{ne^2},\ \eta_\perp=\eta_{//}(1+\Omega_e^2),\ \Omega_e^2=\frac{eB}{q(\nu_{en}+\nu_{ei}+\nu_a)} \tag{9}$$

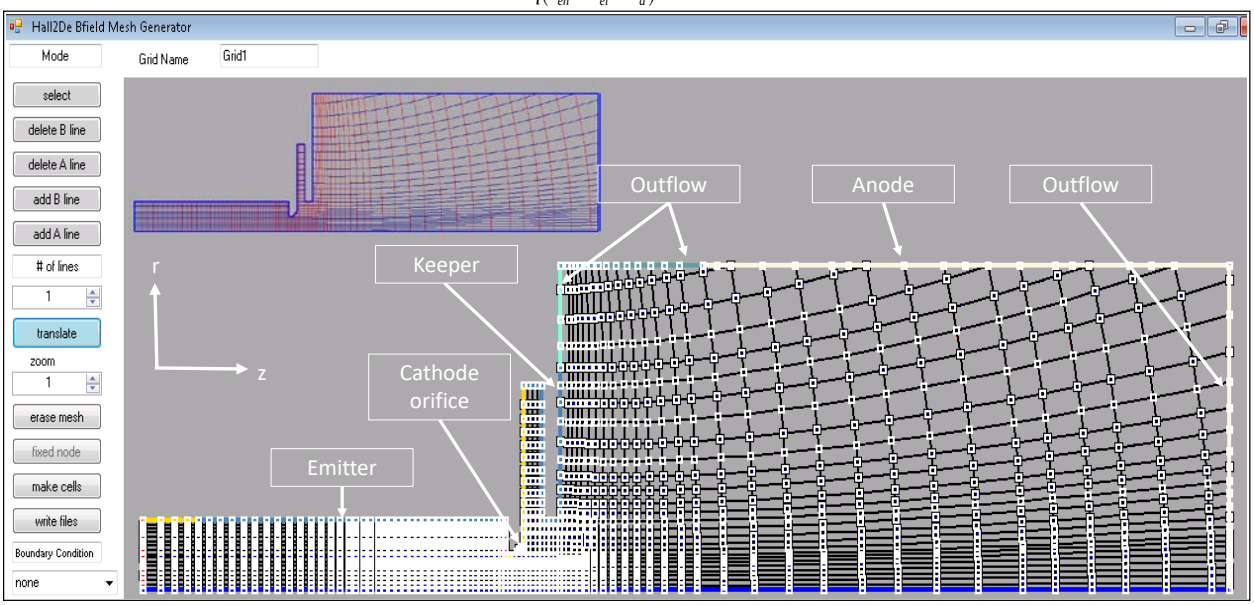

Figure 1. OrCa2D computational domain with boundary conditions. *This particular example employs a magnetic-field-aligned mesh (MFAM) in the cathode plume.*

The computational domain (Fig. 1) comprises the interior of the cathode tube and a considerable section (in the order of tens of centimeters) of the plume, which includes the collecting surface of the anode. The computational domain is designed in a way such that it can replicate the exact conditions at which a cathode test was run in the laboratory. Since a magnetic-field-aligned mesh (MFAM) [20-21] simplifies the solution of Ohm's law, the computational mesh can be made aligned to an applied external magnetic field if one existed in the laboratory test to be replicated or if the aim is to understand plasma parameters when the cathode is operated with a Hall thruster.

Boundary conditions need to be imposed at each surface and also at the outflow. Boundary conditions for a conductor surface are used at the emitter, orifice, keeper, and anode. These conditions assume a infinitesimally small sheath that can be modeled as one-dimensional. The ion and electron current to the surface are determined by:

$$\mathbf{j}_i\cdot\hat{\mathbf{n}}=-\mathbf{j}_n\cdot\hat{\mathbf{n}}=\max\left(0.607n_e e\sqrt{\frac{eT_e}{m_i}},en_e\mathbf{u}_\mathbf{i}\cdot\hat{\mathbf{n}}\right), \tag{10}$$

$$\mathbf{j}_e\cdot\hat{\mathbf{n}}=-\mathbf{j}_e^{ab}\cdot\hat{\mathbf{n}}=-n_e\sqrt{\frac{eT_e}{2\pi m_e}}\exp\left(-\frac{\phi-\phi_b}{T_e}\right), \tag{11}$$

where ϕ_b is the voltage of the conducting surface. In addition, the total electron current from the emitter is the difference between the emitted and absorved current. The emitted current is determined by the Richardson-Dursham [22] emission equation

$$\mathbf{j}_e \cdot \hat{\mathbf{n}} = \left(\mathbf{j}_e^{em} - \mathbf{j}_e^{ab}\right) \cdot \hat{\mathbf{n}}, \quad \mathbf{j}_e^{em} \cdot \hat{\mathbf{n}} = \alpha T_w^{\,2} \exp\left[-\frac{e\left(\varphi_{WF} - \varphi_{SH}\right)}{kT_w}\right]. \tag{12}$$

In the LaB_6 cathode, the emitter temperature and work function are determined by

$$\begin{aligned} T_w &\equiv T_w^0 + c_1 L_{em}\left(\bar{z} - 1\right) + c_2 L_{em}^{\;2}\left(\bar{z}^2 - 1\right) + c_3 L_{em}^{\;3}\left(\bar{z}^3 - 1\right) + c_4 L_{em}^{\;4}\left(\bar{z}^4 - 1\right), \quad \bar{z} = z / L_{em} \\ \varphi_{WF} &\equiv 2.67V. \end{aligned} \tag{13}$$

The emitter temperature profile was measured in the laboratory, while the cathode was in operation, and the coefficients c in Eq. (14) determined to fit the experimental profile. The work function value was obtained from [23] and the modeling of the Shottky effect, φ_{SH}, can be found in [16].

A. Evolution equation for the anomalous collision frequency

The anomalous collision frequency, ν_a, was previously specified in accordance with the model of Sagdeev and Galev [17],

$$\nu_a = \alpha \omega_{pi} M_e \sim \omega_{pi} \frac{u_e}{c_s} \sim \sqrt{\frac{n_e}{T_e}} u_e. \tag{14}$$

This model assumes that the turbulence has reached a saturation state in which the growth of the instability is compensated by nonlinear damping mechanisms. It has been shown that this expression for the anomalous collision frequency is able to acceptably replicate qualitative features of the plasma discharge in the cathode plume [15, 16]. However, the assumptions made by the Sagdeev-Galev model are not met in those regions in which the instability is initiated and develops (i.e., before the saturation state is reached).

We propose here the use of a model that accounts for the development of the instability and that is derived from kinetic theory. A more detailed explanation of the derivation of this model is found in the first part of this article [19]. We start with a kinetic equation for the wave action, a variable that accounts for the magnitude of the instability as a function of time, location, and wave-length

$$\frac{\partial N_k}{\partial t} + \nabla \cdot \left(N_k \nabla_{\mathbf{k}} \omega\right) - \nabla_{\mathbf{k}} \cdot \left(N_k \nabla \omega\right) = 2\gamma N_k, \tag{15}$$

$$\omega = \sqrt{\frac{eT_e}{m_i}} k + \mathbf{u}_i \cdot \mathbf{k} = c_s k + \mathbf{u}_i \cdot \mathbf{k}, \tag{16}$$

$$\gamma = \sqrt{\frac{\pi}{8}} c_s k \left(\left(\frac{m_e}{m_i}\right)^{1/2} \left(\frac{\left(\mathbf{u}_e - \mathbf{u}_i\right) \cdot \mathbf{k}}{c_s \,|\, \mathbf{k} \,|} - 1 \right) - \left(\frac{T_e}{T_i}\right)^{3/2} \exp\left(-\frac{T_e}{2T_i} \right) \right) - \nu_{in}. \tag{17}$$

ω and γ are the frequency and growth rate of the oscillations of wave-length $\mathbf{k}$, respectively, and are directly derived from the dispersion relation of the ion-acoustic instability. The frequency ω accounts for the ion drift in the laboratory frame. The growth rate has a positive term, which accounts for the ratio between the electron-ion drift and the sound speed and that is similar to that found in the Sagdeev-Galev model (14), since $\mathbf{u}_e >> \mathbf{u}_i$, and damping terms that account for Landau damping and the effect of collisions, respectively. Eq. (17) is valid in the limit of $|\mathbf{k}|\lambda_D << 1$. The anomalous transport is assumed to only depend on quantities averaged over the entire spectra of wave-lengths. In particular, following the treatment of Sagdeev and Galev [17], if the turbulent wave energy has an inverse power law dependence $W \sim 1/\omega$, it is possible to find the following simplified expression for the anomalous collision frequency as a function of the wave energy density, W_T:

$$\nu_a \approx 0.01 \omega_{pe} \frac{W_T}{n_e T_e}. \tag{18}$$

In turn, the total wave energy density can be directly derived from the wave action as

$$W_T = \int c_s k N_k \, d\mathbf{k}, \tag{19}$$

Using the definition of wave energy density above, we reach to an evolution equation in the form of a partial differential equation for the wave energy density,

$$\frac{\partial W_T}{\partial t}+\nabla\cdot\left(\left(c_s\frac{\mathbf{k}}{k}+\mathbf{u}_i\right)W_T\right)=\left(2\sqrt{\frac{\pi}{8}}\omega_0\left(\left(\frac{m_e}{m_i}\right)^{1/2}\left(\frac{(\mathbf{u}_e-\mathbf{u}_i)\cdot\mathbf{k}}{c_s|\mathbf{k}|}-1\right)-\left(\frac{T_e}{T_i}\right)^{3/2}\exp\left(-\frac{T_e}{2T_i}\right)\right)-\nu_{in}\right)W_T. \tag{20}$$

This equation has in fact the form of a conservation statement and can be solved concurrently with the remainder of evolution equations (1-8). After the wave energy density is computed at each time step, the anomalous collision frequency is recovered from (18). ω_0 is a cut-off frequency that models the maximum wave-length at which growth of the instability occurs. It has been observed in experimental measurements that the spectra of the IAT is in fact bounded by a maximum value of **k** that has a spatial dependence. In numerical simulations, we make the simplification that ω_0 is constant and use it as a parameter to produce numerical simulations with values of discharge current and voltage that are in agreement with experimental tests.

III. Comparison between anomalous collision frequency models and experiments

The numerical results shown in this article are for a LaB_6 cathode operating at 140 A of discharge current and a mass flow rate of 10 sccm (0.9765 mg/s) of xenon. Refering to Fig. 1, the anode is located 3 cm downstream of the keeper surface and is of cylindrical shape, with an inner radius of 2.2 cm. This 3-cm gap allows for the insertion of probes for plasma measurements in the cathode plume. Measurements of the wave energy density based on the amplitude of the plasma oscillations were also obtained in this region. The discharge voltage during laboratory test in these conditions was 25.2 V. We considered that the maximum emitter temperature is 1733 C, at a location of approximately two-thirds of the length of the emitter. The emitter temperature close to the orifice wall is 1625 C. These values were derived from emitter temperature measurements for a slightly different operating condition (100 A – 12 sccm) [16]. The keeper was operated in floating mode.

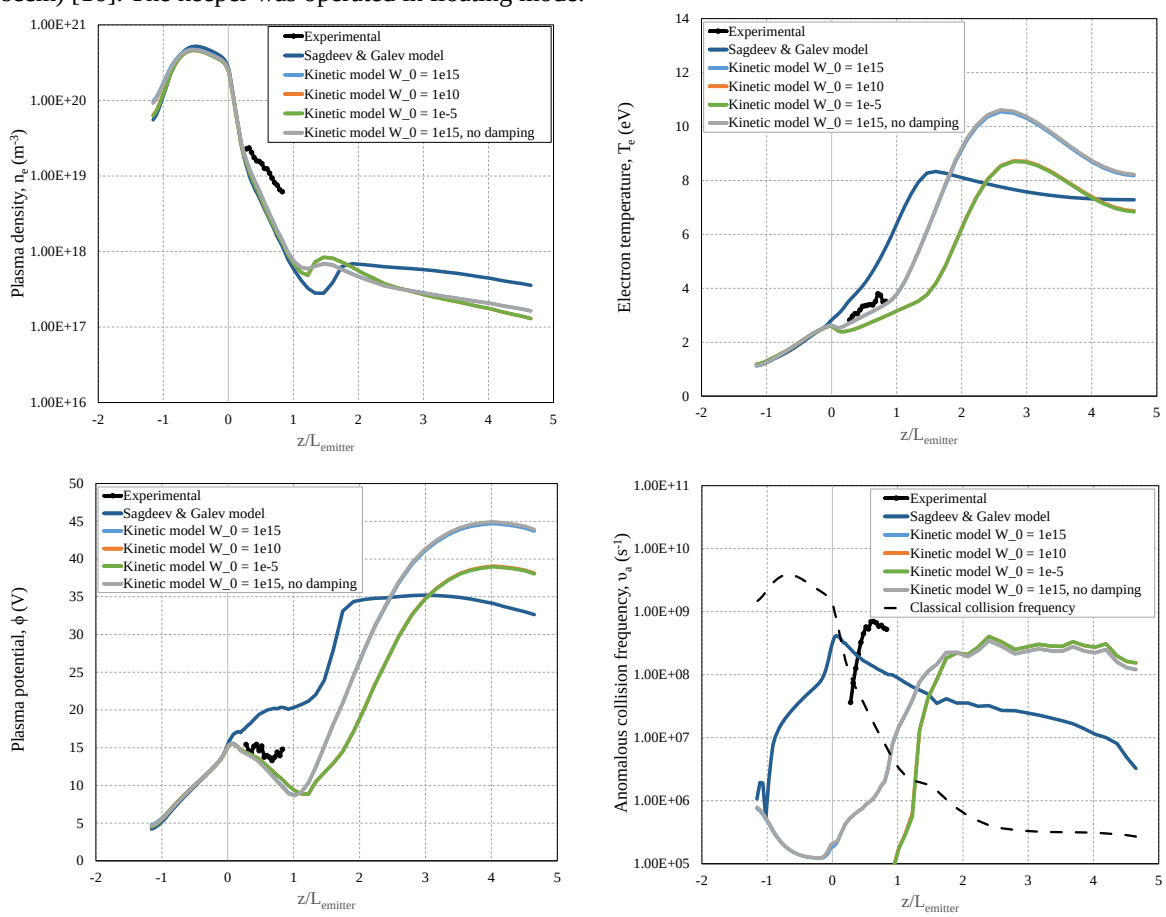

Figure 2. Plasma properties along cathode centerline. *Plasma density (top-left), electron temperature (top-right), plasma potential (bottom-left), and anomalous collision frequency (bottom-right). Results from numerical simulations and experimental measurements are shown. Results for $W_0=10^{10}$ and $W_0=10^{-5}$, and W_0 with and without Landau damping are almost indistinguishable.*

We present in Fig. 2 the computed values of plasma density, electron temperature, plasma potential, and anomalous collision frequency along the cathode centerline. These results have been obtained using the model by Sagdeev and Galev (14) and the kinetic approach (20) for the computation of the anomalous collision frequency. Experimental measurements at the plume region are provided for comparison. z=0 is the cathode orifice entrance and the z-axis has been non-dimensionalized with the emitter length. While solving the energy density equation (20), it is necessary to specify a floor value for W_T. This is because the right-hand side of the equation is negative inside the cathode tube, which will result in $W_T \rightarrow 0$ as $t \rightarrow \infty$. When this happens, there cannot be growth even in regions where the growth rate is positive due to the convective nature of Eq. (20). We have included results produced by three different values of the wave energy density floor W_0. The physical significance of W_0 is that it represents the random thermal motion of the ions spontaneously exciting acoustic modes. We also show a result in which the Landau damping term was removed from Eq. (20). The experimental value of the anomalous collision frequency has been derived from direct experimental measurements of the plasma density, electron temperature, and wave energy density using Eq. (18). The experimental wave energy density is based on direct measurements of the spectra of plasma oscillations [13] and has a factor-of-two uncertainty. We have also included in the Fig. 2 (right-bottom), the profile of the classical collision frequency $\nu_{ei} + \nu_{en}$ obtained from numerical simulation to highlight the regions of the computational domain in which the anomalous collision frequency is the principal contributor to electron transport.

We observe sharp differences in the distribution of anomalous collision frequency along the cathode centerline depending on the model employed. The Sagdeev and Galev model predicts a peak in anomalous transport at the orifice while the kinetic approach predicts rapid growth in the orifice and saturation at approximately 1.5-emitter lengths from the peak of the Sagdev and Galeev model. An explanation for such differences can be found by observing the nature of Eqs. (14) and (20). Equation (14) is an algebraic expression that predicts large values of anomalous transport in regions in which the electron Mach number (the ratio of the drift velocity and the thermal velocity) and the plasma frequency are large. Fig. 3 shows the 2-D distribution of these variables in a numerical simulation with the Sagdeev-Galev model. As the Mach number and plasma density increase and decrease, respectively, along the z-axis, the maximum anomalous collision frequency is achieved at the orifice. On the contrary, Eq. (20) predicts large values of the growth rate when the electron Mach number is large. In the kinetic model, the wave energy density is still small at the orifice since the conditions for growth are not met inside the cathode tube. Thus, the growth rate is maximum at the orifice and immediately downstream of it but, due to the convective term, the peak in the anomalous collision frequency occurs further into the plume than with the Sagdev-Galeev model. The experimental data show a peak that is located in between the results of the two models. The most evident effect in the plasma properties of using the kinetic model is a characteristic kink in the plasma potential between $z/L_{em}=0$ and $z/L_{em}=1$ that does not occur when the Sagdeev-Galev model is employed. This feature can be explained by the absence of significant anomalous collision frequency between $z/L_{em}=0$ and $z/L_{em}=1$ in the kinetic model. Thus, the electrons experience low resistivity to their motion in the axial direction and the plasma potential does not have to increase in order to support the electron current to the anode. In the Sagdeev-Galev model, the resistivity in this region is close to its maximum and the plasma potential has to monotically increase to support the transport of electrons. Experimental measurements suggest that the kinetic model produces better agreement than the Sagdeev-Galev model in this region. In the following sections, we will investigate improvements in the physics models included in OrCa2D that will allow for achieving better agreement with the measurements.

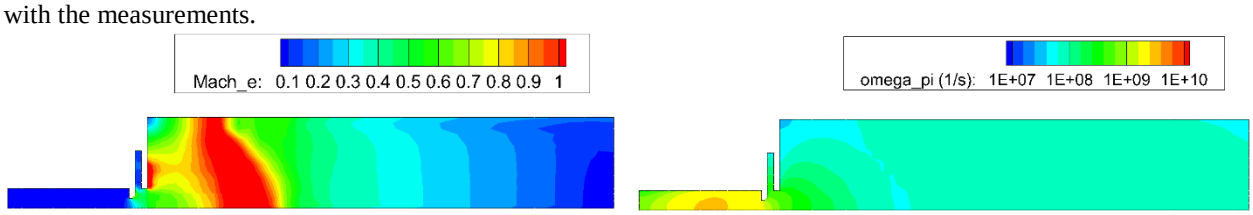

Figure 3. Electron Mach number (left) and ion plasma frequency (right) in a LaB_6 cathode operating at 140 A and 10 sccm. *Sagdeev-Galev model for anomalous collision frequency has been used (results do not change significantly when the kinetic model is considered)*

With respect to the sensitivity of the solution with W_0, we observe that the distribution of the anomalous collision frequency in the plume is almost independent of the choice of floor value. Inside the cathode tube, as long as the anomalous collision frequency is less than the classical collision frequency, the plasma conditions do not change. Irrespectively of W_0, the saturation value at locations that are two emitter lengths downstream of the orifice is the same. The largest differences are found in the growth region (between $z/L_{em}=1$ and $z/L_{em}=2$) and do not affect the plasma properties considerably. The solutions produced by values $W_0=10^{10}$ and $W_0=10^{-5}$ kg/m/s^2/C are almost undistinguishable, while the solution for $W_0=10^{15}$ kg/m/s^2/C exhibits slightly larger plasma potential and electron

temperature values for a given location. Table I summarizes the values of ω_0 in Eq. (20) as a function of W_0, showing that the cut-off frequency used in the simulations are also insensitive to the choice of floor value. The solutions with and without the Landau damping term in Eq. (20) practically overlap each other, suggesting that Landau damping is small in the plume due to large ratio of electron and ion temperatures, computed from Eqs. (5-6).

W_0 (kg/m/s^2/C)	Keeper voltage (V)	ω_0 (1/s)
10^{15}	-7.502	$5.89 \cdot 10^5$
10^{10}	-5.514	$6.47 \cdot 10^5$
10^{-5}	-5.497	$6.49 \cdot 10^5$

Table I. Values of keeper voltage and cut-off frequency (ω_0 in Eq. (20)) as a function of floor wave energy density W_0

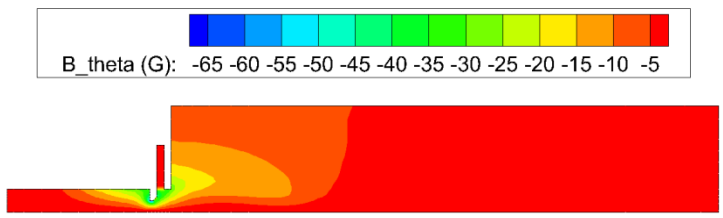

Figure 4. Azimuthal self-induced magnetic field B_θ computed from Eq. (21)

IV. Self-induced magnetic field

The 2-D contours of the plasma density shown in Fig. 2 suggest that the plasma is more confined around the cathode centerline that what the simulation results indicate. A feature that has been neglected in our previous simulations is the presence of a strong self-induced magnetic field due to the large current densities that exist in regions of the cathode with small cross-sections, such as downstream of the cathode orifice exit up to the keeper exit. Fig. 4 shows the 2-D contour of the azimuthal magnetic field produced by the distribution of electron current density found in the simulations of Section III, according to Ampere's law

$$B_\theta(z,r) = \frac{\mu_0}{2r}\int_0^r j_{e,z}(z,r')r'dr'. \tag{21}$$

This expression can be easily evaluated in OrCa2D. The maximum values are found in the vicinity of the orifice and reach more than 50 G. For reference, the typical applied magnetic fields that are measured along the axis of Hall thrusters are in the order of 150 G. We have observed in OrCa2D numerical simulations of centered mounted cathodes with applied magnetic fields that such values completely change the plasma distribution in the plume, making it much more confined around the axis. Thus, we expect that modeling a self-induced ~50 G magnetic field will produce noticeable effects in OrCa2D simulations of high-current cathodes.

We allow only for the azimuthal component of the magnetic field in our modelsince the electron current is mostly axial in the region of interest. This assumption also simplifies the process of solving for Ohm's law in OrCa2D. For a generic magnetic field in three dimensions, which can be the combination of the applied and the self-induced magnetic field, Ohm's law reads

$$\begin{aligned}
&\theta \rightarrow 0 = -\eta\Omega_e j_{e\perp} + \eta j_{e\theta}, \\
&// \rightarrow E_{//} = -\frac{\nabla_{//}(nT_e)}{n} + \eta\Omega_e j_{e\perp}\beta_\theta + \eta j_{e//} + \eta_{ei} j_{i//}, \\
&\perp \rightarrow E_\perp = -\frac{\nabla_\perp(nT_e)}{n} - \eta\Omega_e j_{e//}\beta_\theta + \eta\left(1+\Omega_e^2\beta_{//}^2\right)j_{e\perp} + \eta_{ei} j_{i\perp}.
\end{aligned} \tag{22}$$

In the above expressions, the parallel and perpendicular directions refer to the projection of the magnetic field in the z-r plane. We can invert Ohm's law to obtain closed expressions for the in-plane current density components

$$
\begin{aligned}
j_{e//} &= \frac{1+\Omega_e^2\beta_{//}^2}{\left(1+\Omega_e^2\right)\eta}\left(-\nabla_{//}\phi+\frac{\nabla_{//}\left(nT_e\right)}{n}-\eta_{ei}\,j_{i//}\right)-\frac{\Omega_e\beta_\theta}{\left(1+\Omega_e^2\right)\eta}\left(-\nabla_{\perp}\phi+\frac{\nabla_{\perp}\left(nT_e\right)}{n}-\eta_{ei}\,j_{i_\perp}\right),\\
j_{e\perp} &= \frac{\Omega_e\beta_\theta}{\left(1+\Omega_e^2\right)\eta}\left(-\nabla_{//}\phi+\frac{\nabla_{//}\left(nT_e\right)}{n}-\eta_{ei}\,j_{i//}\right)+\frac{1}{\left(1+\Omega_e^2\right)\eta}\left(-\nabla_{\perp}\phi+\frac{\nabla_{\perp}\left(nT_e\right)}{n}-\eta_{ei}\,j_{i_\perp}\right).
\end{aligned}
\tag{23}
$$

As mentioned in Section II, the grid can be aligned with an applied in-plane magnetic field in order to solve Eqs. (8) and (23) without the negative effects of accounting for cross-diffusion terms. This would be no longer possible if we consider the self-induced magnetic field components in the z-r plane, as the vector β can change from time-step to time-step. Eq. (23) can still be solved in a MFAM if we do not account for an in-plane self-induced magnetic field and in a generalized grid if, in addition, no applied magnetic field exists (i.e., $\beta_{//}$=0). It can also be shown that this expression is equivalent to Eqs. (8-9) when β_θ=0.

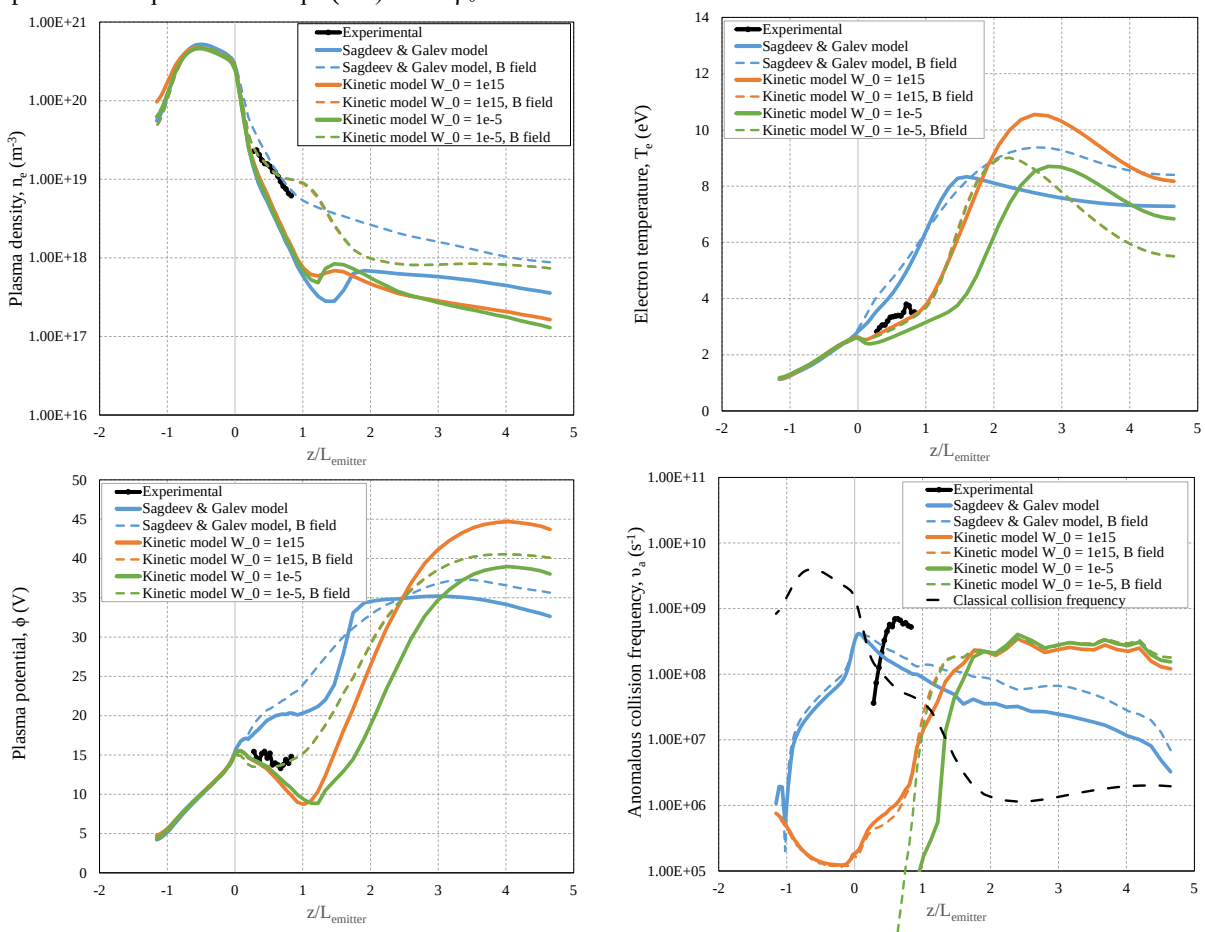

Figure 5. Plasma properties along cathode centerline. Comparison between results with and without self-induced magnetic field. *Plasma density (top-left), electron temperature (top-right), plasma potential (bottom-left), and anomalous collision frequency (bottom-right). Results from numerical simulations and experimental measurements are shown.*

Figure 5 depicts the plasma properties and anomalous collision frequencies that are obtained from numerical simulation when the model for a self-induced magnetic field in the azimuthal direction is included in OrCa2D. We also plot some of the results already in Fig. 2 for comparison. For both anomalous collision frequency models, (14) and (18-20), the plasma density downstream of the cathode orifice increases along the cathode centerline, as a result of the magnetic field. In fact, both models produce reasonably good agreement with the experimental measurements (Fig. 5, upper-left) while in previous simulations the density was underestimated by almost an order of magnitude at z/L_{em} ~1. Figure 6 shows 2-D contours of the plasma density with and without the self-induced magnetic field. It is clear from this figure that the ion beam expands almost isotropically when no magnetic field is present. When the model for B_θ is included, the beam expands predominantly in the axial direction.

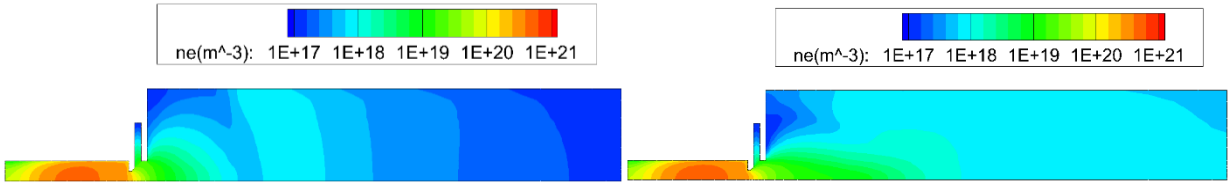

Figure 6. Plasma density in LaB_6 cathode operating at 140 A and 10 sccm without self-induced magnetic field (left) and with self-induced magnetic field (right)

With respect to the anomalous collision frequency, similar trends to those observed in Section III are recovered. The Sagdeev-Galev model predicts a peak in the anomalous collision frequency at the orifice. For the kinetic model, sensitivity to the floor value W_0 is also small. However, the saturation of the anomalous collision frequency occurs upstream compared to the result with no magnetic field. Even though the electron Mach number, which controls the growth rate of Eq. (20) decreases in a more confined beam (i.e., for the same electron current, the plasma density increases resulting in a lower electron drift velocity), the value of the cut-off frequency ω_0 that is required to meet the operating condition of 140 A is higher than the one used in Section III. Thus, a higher value of ω_0 produces a saturation value for ν_a that is approximately the same as that obtained in previous simulations and moves the growth upstream. Even with this improvement, the measured peak of the anomalous collision frequency is still upstream of the location predicted by numerical simulations. We also observe that with the inclusion of the self-induced magnetic field, the electron temperature and plasma potential values agree remarkably well with the experimental measurements.

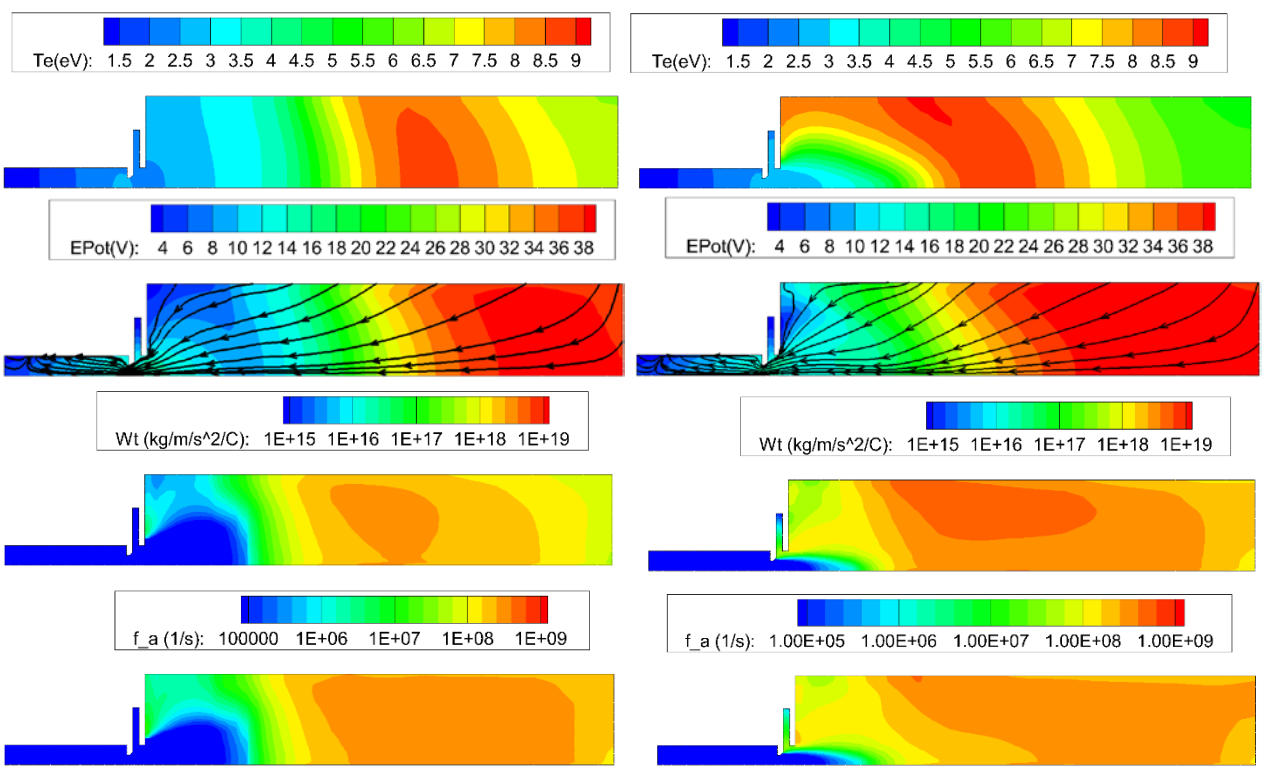

Figure 7. 2-D contour plots for plasma parameters. *Left: no self-induced magnetic field, right: with self-induced magnetic field. From top to bottom: electron temperature, plasma potential with electron drift streamtraces, wave energy density, and anomalous collision frequency.*

Self-induced B-field	W_0 (kg/m/s^2/C)	ω_0 (1/s)
No	10^{15}	$5.89 \cdot 10^5$
Yes	10^{15}	$9.23 \cdot 10^5$
No	10^{-5}	$6.49 \cdot 10^5$
Yes	10^{-5}	$9.24 \cdot 10^5$

Table II. Values of cut-off frequency (ω_0 in Eq. (20)) as a function of floor wave energy density W_0 and inclusion of self-induced magnetic field model

To conclude this section, we show in Fig. 7 the 2-D contours of the relevant plasma parameters in simulations with and without the model for a self-induced magnetic field. The confinement of the plasma around the cathode axis is evident, with plasma properties closely following the plasma density contours of Fig. 6. We also observe that the electron streamtraces are closely parallel to the longitudinal axis for approximately one cathode tube length downstream of the orifice. In the region further downstream the effects of the self-induced magnetic field are negligible, as indicated by the 2-D distribution of B_θ in Fig. 4.

V. Effect of ion heating due to ion-acoustic turbulence

The last effect we explore in this article is ion heating induced by the ion-acoustic turbulence. The IAT produces an increase of the high-energy tail of the ion distribution function, which can in turn be quantified in terms of an increase of the ion temperature. In [18], Jorns et al. showed that, in a linearized model that considers that the ion temperature due to classical effects (5) is much lower than the electron temperature (which is the case in previous simulations, as shown by the weak influence of Landau damping), the main source of heating for ions involved in the ion-acoustic turbulence takes the form

$$\nabla T_i = \nabla\left(\frac{W_T}{n_e}\right), \tag{24}$$

This expression can be numerically integrated in OrCa2D starting from locations inside the cathode tube in which $W_T = W_0$. Eq. (24) then supersedes Eq. (5) as the energy equation for ions while the latter remains the energy equation for the neutrals. The validity of (24), at least for cathodes operating at high-current conditions have been recently confirmed experimentally in [24], where laser induced fluorescence (LIF) was used to determine the distribution function of the ions at multiple axial locations in the cathode plume. The increased ion temperature, which can become comparable to the electron temperature, has the effect of increasing the importance of Landau damping in Eq. (20).

Figure 8 depicts the plasma properties along the axis centerline when anomalous ion heating is considered and a comparison with previous results of Sections III and IV. Figure 9 shows 2-D contour plots of the relevant plasma properties: ion temperature, wave energy density, and anomalous collision frequency. Table III contains the values of the cut-off frequency, ω_0, that we use in our OrCa2D simulations in order to achieve the specified operating condition of 140 A at a mass flow rate of 10 sccm and discharge voltage of 25.2 V.

As shown in Fig. 9, the ion temperature computed from (24) reaches a maximum value of approximately 2 eV along the cathode centerline. At the same location, the solution of Eq. (5) predicts a temperature of 0.02 eV and the electron temperature is between 4 and 6 eV. The Landau damping term in Eq. (20) is maximal when the ratio of the electron to the ion temperature is 3. Thus, when anomalous ion heating is considered, the Landau damping is close to its maximum, while it was negligible in the results shown in Sections III and IV. The 2-D profiles of wave energy density and anomalous collision frequency respond by reaching a maximum value along the thruster centerline that is closer to the cathode than in previous simulations. In addition, the anomalous collision frequency decreases downstream of the peak instead of remaining approximately constant. We can find an explanation to these changes by assuming that, if the discharge current and voltage stay constant, the amount of anomalous resistivity integrated along the electron path between the cathode and anode must remain approximately constant. Since Landau damping decreases the anomalous collision frequency and, in consequence, the resisitivity, we need higher velues of the anomalous collision frequency in locations upstream of where the Landau damping is maximal. The only way to achieve this in our simulations is to increase the cut-off frequency, ω_0, as shown in Table III, to promote growth of the instability. The value of ω_0 obtained in the simulation with ion heating, $6.49 \cdot 10^5$ 1/s, is remarkably similar to the upper bound of the frequency in the experimental data showed in Fig. 3 of [13] for multiple operating conditions. As shown in Fig. 8 (bottom-right), the anomalous collision frequency in simulations with anomalous ion heating closely replicate in location and magnitude the values inferred from experimental measurements. Since there exists an uncertainty factor of two in the the measurements of the wave action from where the experimental anomalous collision

frequency was derived, the computed and experimental values may be indeed closer than shown in Fig. 8. Small changes are also observed in the electron temperature, plasma potential, and plasma density. However, the numerical results still agree reasonably well with the measured quantities.

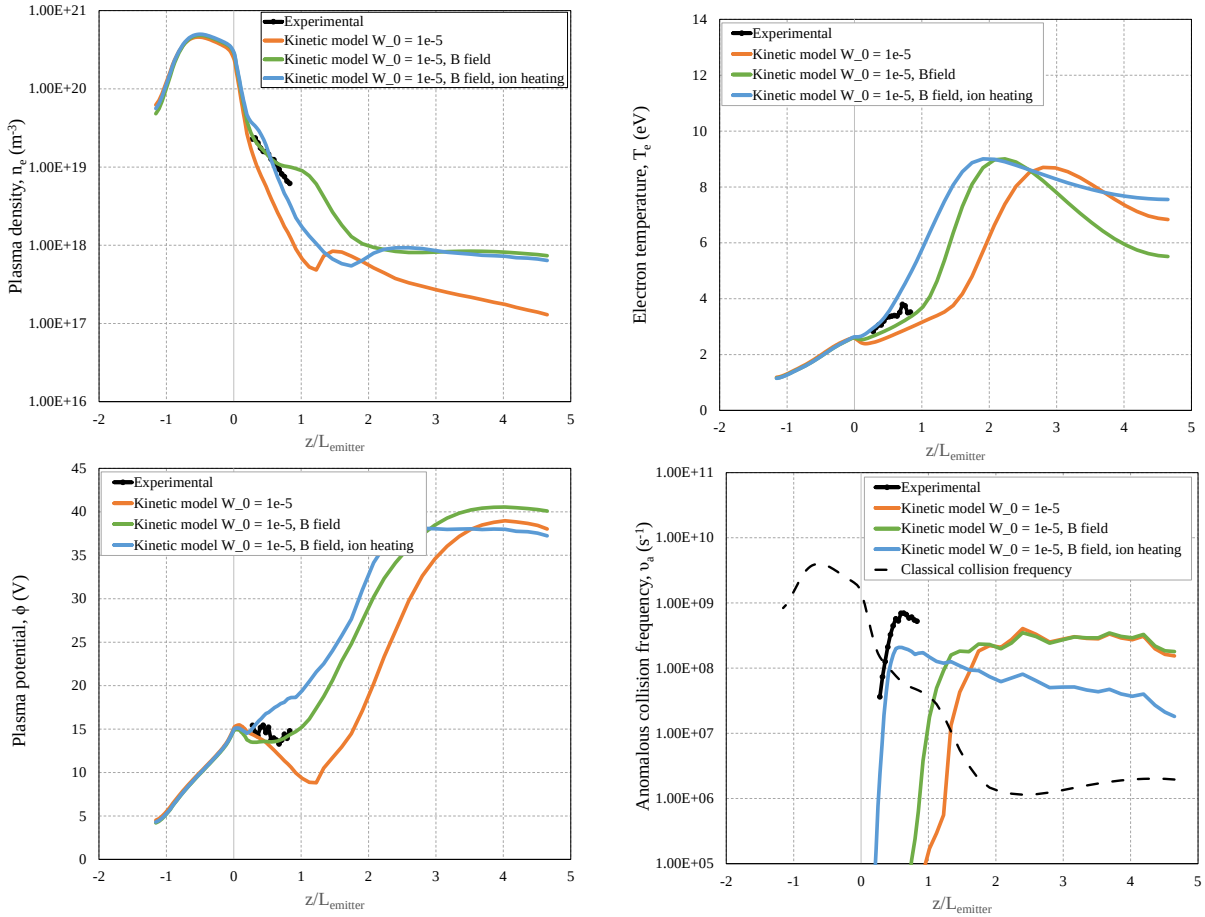

Figure 8. Plasma properties along cathode centerline. Comparison between results with and without self-induced magnetic field and with and without anomalous ion heating. *Plasma density (top-left), electron temperature (top-right), plasma potential (bottom-left), and anomalous collision frequency (bottom-right). Results from numerical simulations and experimental measurements are shown.*

Ion heating	Self induced magnetic field	W_0 (kg/m/s^2/C)	ω_0 (1/s)
No	No	10^{-5}	$6.49 \cdot 10^5$
No	Yes	10^{-5}	$9.24 \cdot 10^5$
Yes	Yes	10^{-5}	$3.39 \cdot 10^6$

Table III. Values of cut-off frequency (ω_0 in Eq. (20)) as a function of inclusion of self-induced magnetic field and ion heating models

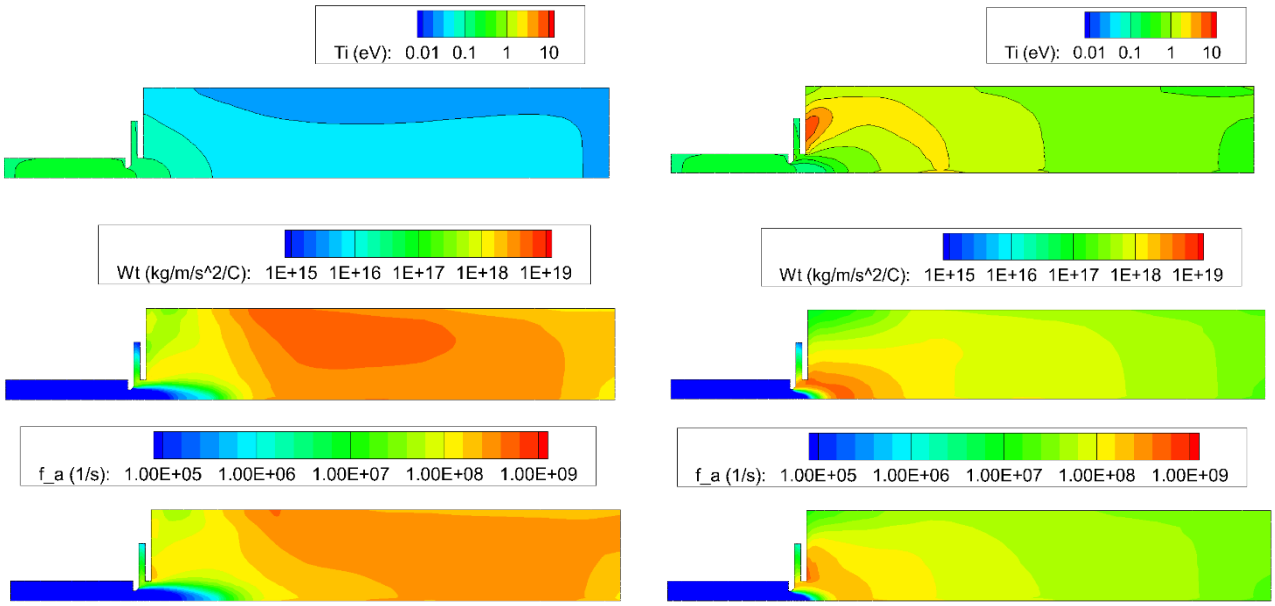

Figure 9. 2-D contour plots for plasma parameters. *Left: no anomalous ion heating, right: with anomalous ion heating. From top to bottom: ion temperature, wave energy density, and anomalous collision frequency.*

VI. Conclusion

We presented in this paper a model, based on kinetic theory, that describes the growth and saturation of the ion-acoustic turbulence (IAT) in the plume of hollow cathodes and its effect on electron mobility and ion heating. We also included the effects of self-induced magnetic fields, which are important in cathodes operating at large discharge currents. Numerical simulations that employed these models show large improvements in our agreement with experimental measurements with respect to a previous model, which assumed complete saturation of the instability and did not account for the growth stage of the instability.

The total wave energy density was derived from kinetic theory and computed as the solution of a partial differential equation (PDE) that is hyperbolic in nature, with a convection term depending on the group velocity and a right-hand side term that controls the local growth or damping of the instability. The transport and growth coefficients in the PDE were extracted from the linearized dispersion relation of the ion-acoustic instability. This equation can be solved concurrently with the equations of motion of neutrals, ions, and electrons in the hollow cathode code OrCa2D. The increased resistivity due to IAT can be derived from the wave energy density be means of an algebraic expression. The results produced by this model and its predecessor were compared with experimental measurements in the plume of a LaB_6 cathode operating at a discharge current of 140 A and mass flow rate of 10 sccm. The saturation model consistently predicted that the resisitivity of electrons peaked at the cathode orifice while the model based on the wave energy density predicted the growth rate of the instability being maximum at the cathode orifice but the resistivity reaching a maximum value downstream in the plume. The experimental measurement of the electron resistivity predicted a peak located between the two numerical results.

Further improvements to the agreement with plasma measurements were made by including a model for the effect of the self-induced magnetic field. It was shown that in hollow cathodes operating at large discharge currents, Ampere's law must be included in the equations governing the evolution of the plasma. In turn, Ohm's law must be modified accordingly to account for the cross terms that result from the presence of an azimuthal magnetic field. Accounting for the magnetic field resulted in numerical solutions that showed significant plasma confinement in the proximity of the cathode centerline downstream of the orifice, in agreement with expertimental observations.

Finally, we presented a linear model that accounts for ion heating as a function of the wave energy density. This model was recently validated by experimental measurements of the ion temperature and magnitude of the wave oscillations in the cathode plume. Large ion temperatures magnify the relevance of Landau damping. Numerical results that accounted for anomalous ion heating predicted that the maximum resistivity to the motion of electrons, computed from the model based on the wave energy density, occurs at the exact same location that was inferred from direct experimental measurements. This is in contrast to our previous simulations for which anomalous ion heating was not accounted.

Acknowledgments

The research described in this paper was carried out by the Jet Propulsion Laboratory, California Institute of Technology, under a contract with the National Aeronautics and Space Administration. The support of NASA's Space Technology Mission Directorate through the Solar Electric Propulsion Technology Demonstration Mission (SEP TDM) project is gratefully acknowledged.

References

[1] J. R. Brophy, L. Friedman, and F. Culick, "Asteroid Retrieval Feasibility," in Aerospace Conference, 2012, Big Sky, MT, 2012, pp. 1 – 16.

[2] J. R. Brophy, and S. Oleson, "Spacecraft conceptual design for returning entire near-Earth asteroids", AIAA Paper No. 2012-4067, in Proceedings of the 48th AIAA Joint Propulsion Conference, Atlanta, GA, 2012, pp. 4067.

[3] J. E. Polk, J. Anderson, J. Brophy, V. Rawlin, M. Patterson, J. Sovey, and J. Hamley, "An overview of the results from an 8200-hour wear test of the NSTAR ion thruster", AIAA paper no. 99-2446, in proceedings of the 35th AIAA Joint Propulsion Conference, Los Angeles, CA, 1999

[4] A. Sengupta, J. R. Brophy, and K. D. Goodfellow, "Status of the extended life test of the Deep Space I flight spare ion engine after 30,352 hours of operation", AIAA paper 03-4558, in proceedings of the 39th AIAA Joint Propulsion Conference, Huntsville, AL, 2003

[5] D. M. Goebel, K. K. Jameson, I. Katz and I. G. Mikellides, "Plasma potential behavior and plume model transitions in hollow cathode discharges", IEPC-2007-277, in proceedings of the 30th International Electric Propulsion Conference, Florence, Italy, 2007.

[6] I. G. Mikellides, I. Katz, D. M. Goebel, J. E. Polk, and K. K. Jameson, "Evidence of non-classical plasma transport in hollow cathodes for electric propulsion", Journal of Applied Physics, Vol. 101, No. 6, 2007, 063301

[7] I. G. Mikellides, I. Katz, D. M. Goebel, and J. E. Polk, "Theoretical model of a hollow cathode insert plasma", AIAA paper 2004-3817, in proceedings of 40th AIAA/ASME/SAE/ASEE Joint Propulsion Conference, Fort Lauderdale, FL, 2004.

[8] I. G. Mikellides, I. Katz, D. M. Goevel, and J. E. Polk, "Hollow cathode theory and experiment II: A two-dimensional theoretical model of the emitter region", Journal of Applied Physics, Vol. 98, No. 11, 2005, 113303

[9] V. Bychenkov, V. Silin, and S. Uryupin, "Ion-acoustic turbulence and anomalous transport", Physics Reports Vol. 164, Issue 3, 1988, 199-215.

[10] H. de Kluvier, N. F. Perepelkin, and A. Hirose, "Experimental results on current-driven turbulent plasmas – a survey", Physics Reports, Vol. 199, Issue 6, 1991, 281-381.

[11] T. H. Stix, "Waves in Plasmas", Springer-Verlag, New York, 1992

[12] W. Horton, "Turbulent transport in magnetized plasmas", World Scientific, Singapore, 2012.

[13] B. A. Jorns, I. G. Mikellides, and D. M. Goebel, "Ion acoustic turbulence in a 100-A LaB6 hollow cathode", Physical Review E, Vol. 90, 2014, 063106.

[14] I. G. Mikellides and I. Katz, "Wear mechanisms in electron sources for ion propulsion I: neutralizer hollow cathode", Journal of Propulsion and Power, Vol. 24, No. 4, 2008, 855-865

[15] I. G. Mikellides, I. Katz, D. M. Goebel, K. K. Jameson and J. E. Polk, "Wear mechanisms in electron sources for ion propulsion II: discharge hollow cathodes", Journal of Propulsion of Power, Vol. 24, No 4, 2008, 866-879

[16] I. G. Mikellides, D. M. Goebel, B. A. Jorns, J. E. Polk, and P. Guerrero, "Numerical simulations of the partially-ionized gas in a 100-A LaB6 hollow cathode", IEEE Transactions on Plasma Science, Special Issue on Plasma Propulsion, Vol. 43, No. 1, 2015, pp. 173-184.

[17] R.Z. Sagdeev, A. Galeev, Nonlinear plasma theory, W. A. Benjamin, New York, 1969.

[18] B. A. Jorns, I. G. Mikellides, D. M. Goebel, and A. Lopez Ortega, "Mitigation of energetic ions and keeper erosion in a high-current hollow cathode", IEPC-2015-134, in proceedings of the 34th International Electric Propulsion Conference, Hyogo-Kobe, Japan, 2015.

[19] B. A. Jorns, A. Lopez Ortega, and I. G. Mikellides, "First-principles modeling of IAT-driven anomalous resistivity in hollow cathodes discharges I: Theory", AIAA paper 2016-xxxx, in proceedings of the 52nd AIAA Joint Propulsion Conference, Salt Lake City, UT, 2016.

[20] R. Marchand and M. Dumberry, "CARRE: a quasi-orthogonal mesh generator for 2D edge plasma modelling", Computer Physics Communications, Vol. 96, 1996, pp. 232-246.

[21] Z. Lin, T. S. Hahm, W. W. Lee, W. M. Tang, and R. B. White, "Turbulent Transport Reduction by Zonal Flows: Massively Parallel Simulations," Science, Vol. 281, 1998, pp. 1835-1837.

[22] S. Dusham, "Electron emission from metals as a function of temperature", Physical Review, Vol. 21, No. 6, 1923, 623-636

[23] E. K. Storms and B. A. Mueller, "Study of surface stoichiometry and thermionic emission using LaB_6", Journal of Applied Physics, Vol. 50, No. 5, 1979, 3691-3698.

[24] C. A. Dodson, D. Perez Grande, B. A. Jorns, and D. M. Goebel, "Laser-induced fluorescence measurements of energetic ions in a 100-A LaB_6 hollow cathode", AIAA paper 2016-xxxx, in proceedings of the 52nd AIAA Joint Propulsion Conference, Salt Lake City, UT, 2016.